Received 4 March 2026, accepted 29 March 2026, date of publication 6 April 2026, date of current version 9 April 2026.
Digital Object Identifier 10.1109/ACCESS.2026.3681397

RESEARCH ARTICLE

Endogenous Interface Pricing for Consistent Transmission–Distribution Co-Optimization With Discrete Distribution Controls

SEUNG-GIL NOH[1], (Student Member, IEEE), MIGUEL HELENO[2], (Senior Member, IEEE), AND YUN-SU KIM[3], (Senior Member, IEEE)
[1]Graduate School of Energy Convergence, Gwangju Institute of Science and Technology (GIST), Gwangju 61005, South Korea
[2]Lawrence Berkeley National Laboratory, Berkeley, CA 94720, USA
[3]Department of Electrical Engineering and Computer Science, Gwangju Institute of Science and Technology (GIST), Gwangju 61005, South Korea
Corresponding author: Yun-Su Kim (yunsukim@gist.ac.kr)

This work was supported by the Korea Institute of Energy Technology Evaluation and Planning (KETEP) and the Ministry of Trade, Industry and Energy (MOTIE) of the Republic of Korea (No. RS-2024-00394225).

ABSTRACT This paper proposes an endogenous interface pricing model for day-ahead transmission–distribution co-optimization that co-determines the interface locational marginal price (LMP) and the transmission–distribution exchange, ensuring price–dispatch consistency while optimally scheduling discrete distribution controls. The formulation couples a DC optimal power flow (OPF) with a branch-flow AC OPF that schedules distributed energy resources (DERs), tap-changer settings, capacitor banks (CBs), and multi-period energy storage systems (ESSs) under feeder voltage and current limits, and is solved as a mixed-integer second-order cone program (MISOCP). In a T14–D33 system, coordinated device scheduling recovers about 90% of the distribution-to-transmission export achievable in a reference case that ignores distribution network (DN) limits, while satisfying a 1.05 p.u. voltage upper bound. In a T39–D34/D37/D123 system, a sequential decoupled benchmark produces interface LMP distortions up to 12.5% and a 7.28% mismatch in net export energy, whereas the proposed model removes these distortions and the associated settlement mismatches. Second-order cone (SOC) relaxation gaps remain below 10^{-3} in all cases.

INDEX TERMS Transmission–distribution co-optimization, endogenous interface pricing, price-dispatch consistency, discrete distribution controls, bilevel optimization.

I. INTRODUCTION

A. BACKGROUND AND MOTIVATION

Modern distribution networks (DNs) are transitioning from passive load serving networks to actively managed subsystems due to the rapid growth of distributed energy resources (DER) such as photovoltaic (PV) generation, wind generation, and energy storage [1], [2], [3]. High penetration of DERs can trigger voltage rise, reverse power flow, and thermal congestion, so feeder operating limits become binding more frequently. Distribution system operators (DSOs) therefore schedule discrete voltage control devices such as on-load tap changers (OLTCs), step-voltage regulators (SVRs), and capacitor banks (CBs) together with inverter reactive power support and energy storage systems (ESSs) [4], [5], [6], [7], [8], [9], [10]. In parallel, energy management research in microgrids increasingly relies on data-driven forecasting and control pipelines [11]. These approaches improve adaptivity, but market clearing and interface scheduling still require network constraints consistent with power flow physics and marginal prices that remain economically interpretable.

A common simplification is to represent the upstream transmission network (TN) as an electrically decoupled infinite bus and to treat the point of common coupling (PCC) locational marginal price (LMP) as fixed. Sequential TN-DN clearing can then create a mismatch between the PCC LMP and the scheduled exchange because the DN-feasible response changes the net injection at the interface and

The associate editor coordinating the review of this manuscript and approving it for publication was Cuo Zhang.

therefore the marginal conditions seen by the TN. The problem becomes more severe when feeder limits are binding, discrete controls restrict deliverable flexibility, and uncertainty or multi-product settlement requires ex post interface adjustments.

Prior work addresses parts of this challenge. Interface feasible regions and time coupled flexibility sets at the PCC have been quantified to support transmission and distribution coordination [12], [13]. Operational and regulatory studies also show that inverter reactive power control and CB switching can support upstream voltage and that interface setpoints can be tracked while honoring internal distribution constraints [14], [15], [16]. On the market side, coordinated frameworks between independent system operators (ISO) and DSOs have been formulated using stochastic optimization, equilibrium models, and hierarchical market mechanisms [17], [18], [19], [20], [21]. Distribution LMP based hierarchical scheduling models have also been developed to price distribution flexibility [22]. Convex relaxation based coordinated operation has been studied in integrated energy systems with sector coupled resources [23]. However, many market clearing formulations represent distribution feasibility using aggregated interface models and do not explicitly schedule feeder discrete devices, which can be critical in multi-product settings where discrete actions determine deliverable flexibility at the interface. Several studies also treat the interface price as fixed during distribution scheduling, which can leave settlement distortions when the distribution schedule changes marginal conditions at the interface.

Recent uncertainty and risk aware models further highlight the importance of robust and stochastic decision making. Hybrid robust and stochastic nodal pricing with electric vehicle (EV) charging stations has been proposed in [24], and risk-based bi-level integration of a DSO with prosumers and parking lots under upper market involvement has been studied in [25]. Broader risk aware formulations also include P-robust peer-to-peer trading in multi energy microgrids and P-robust transmission planning to increase renewable hosting capacity [26], [27]. These works provide valuable uncertainty modeling insights, but they do not co-determine the LMP at the PCC together with a distribution feasible schedule that includes discrete feeder devices under alternating current power flow constraints.

Embedding alternating current power flow physics in coordinated market models remains challenging because AC optimal power flow (OPF) is nonconvex. Convexification techniques include semidefinite programming (SDP) relaxations, second-order cone programming (SOCP) relaxations such as branch flow models, quadratic convex (QC) relaxations, and McCormick envelope tightening for bilinear terms [28], [29], [30], [31], [32]. These approaches differ in exactness conditions and computational scaling. SDP and QC relaxations can be tighter, but they are often heavier in large scale settings, particularly when mixed-integer device models are included. This paper therefore adopts a second-order cone (SOC) relaxed branch-flow model to tractably schedule discrete feeder devices while co-determining the interface price and scheduled exchange under DN-feasible operation.

Table 1 contrasts prior work by showing that market-oriented studies often simplify DN feasibility, feeder-level studies typically do not jointly determine the PCC price and power exchange, and risk-aware models rarely integrate discrete feeder controls with AC-feasible scheduling.

B. SCOPE AND CONTRIBUTIONS

This paper proposes an endogenous interface pricing model for day-ahead TN-DN co-optimization of active DNs with discrete voltage-control devices and energy storage. The TN is modeled by a DC-OPF, and each DN by a multi-period SOCP-relaxed branch-flow AC-OPF with OLTC and SVR taps, staged CB switching, ESS state-of-charge dynamics, and feeder voltage and current limits. PCC active-power exchange is bidirectional. Ancillary-service procurement, dynamic-stability constraints, security-constrained formulations, and uncertainty and reserve co-optimization are outside the scope of the base model and are left for future work.

The main contributions are as follows:

1) **Settlement-consistent endogenous PCC pricing:** PCC price and exchange are co-determined through primal-dual embedding of the DC-OPF, eliminating the price-dispatch inconsistency of sequential clearing.
2) **Feeder-level discrete DN scheduling under AC feasibility:** exact binary encodings capture OLTC and SVR tap positions, together with staged CB switching, within a multi-period SOCP branch-flow AC-OPF with ESS dynamics.
3) **Tractable single-level reformulation:** the coordinated TN-DN model is reformulated as a mixed-integer second-order cone program (MISOCP) using Karush–Kuhn–Tucker (KKT) conditions, strong duality, and linearized complementarity.
4) **Tight SOC relaxation in practice:** a hybrid penalty and sequential refinement scheme reduces relaxation slack and yields small SOC gaps in the case studies.

Case studies on modified IEEE TN-DN systems quantify the operational value of active DN control under binding feeder limits. They also show that endogenous interface pricing removes the PCC LMP distortions caused by sequential decoupled clearing while preserving DN-feasible operation.

C. PAPER STRUCTURE

The remainder of this paper is organized as follows. Section II describes the system structure and formulates the endogenous interface pricing co-optimization problem based on the DC-OPF and the SOCP branch-flow AC-OPF with discrete controls and ESS dynamics. Section III presents the single-level reformulation and the solution methodology, including the treatment of discrete variables and the assessment and refinement of SOC relaxation gaps. Section IV

TABLE 1. Summary of representative related studies and comparison with the proposed work.

Reference	TN model	DN AC model	Endog. PCC price	Endog. PCC power	Discrete DN controls	ESS multi-period	Unc. /risk	Convex. relax.	Multiple markets
Representative DN device coordination [4]–[10]	–	△	–	–	✓	△	–	△	–
PCC flexibility region and mapping [12], [13]	–	✓	–	△	△	△	△	✓	–
ISO–DSO coordinated market participation under uncertainty [17]	✓	△	✓	✓	–	△	✓	✓	✓
Distribution market clearing and pricing with ISO coordination [18]	✓	✓	✓	✓	–	–	–	✓	–
Hierarchical distribution LMP tri-level scheduling [22]	–	△	△	△	–	△	–	△	–
SOCP-based coordinated operation in integrated energy systems [23]	–	△	–	–	–	△	–	✓	–
Hybrid robust/stochastic DN nodal pricing with EV charging [24]	–	✓	△	△	–	✓	✓	–	–
Risk-based bi-level DSO integration with prosumers and parking lots [25]	△	✓	△	△	–	✓	✓	–	✓
P-robust peer-to-peer framework for multi-energy microgrids [26]	–	△	△	△	–	△	✓	△	✓
P-robust transmission planning with TCSC [27]	✓	–	–	–	–	–	✓	✓	–
Data-driven EMS survey [11]	–	–	–	–	–	△	△	–	–
This work (proposed)	✓	✓	✓	✓	✓	✓	–	✓	–

Note: ✓ denotes that the feature is explicitly modeled and co-optimized; △ denotes partial or indirect treatment; – denotes that the feature is not considered.

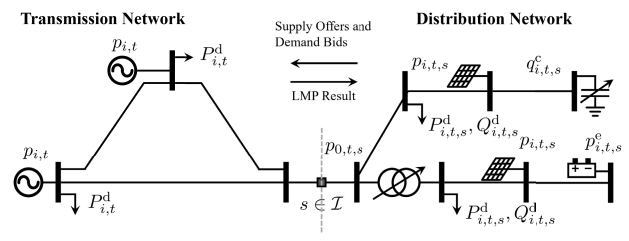

FIGURE 1. Structure of the transmission network and distribution networks with control devices.

reports the case studies and discusses operational and economic implications, including PCC LMP deviations under sequential decoupled co-optimization. Section V concludes the paper.

II. PROBLEM FORMULATION

A. STRUCTURE OF THE TRANSMISSION AND DISTRIBUTION NETWORKS

Fig. 1 illustrates the integrated TN–DN structure with distribution-level control devices. The TN is represented by the bus set $\mathcal{B}^{\mathrm{T}}$ and the line set $\mathcal{L}^{\mathrm{T}}$. The generator and demand bus sets are denoted by $\mathcal{G}^{\mathrm{T}} \subseteq \mathcal{B}^{\mathrm{T}}$ and $\mathcal{D}^{\mathrm{T}} \subseteq \mathcal{B}^{\mathrm{T}}$, respectively. The set of DNs connected to the TN is denoted by $\mathcal{I}$. Each DN $s \in \mathcal{I}$ is modeled by the bus set $\mathcal{B}^{\mathrm{D}}_s$ and the line set $\mathcal{L}^{\mathrm{D}}_s$. The sets of buses in DN s equipped with DERs, demands, CBs, and ESSs are denoted by $\mathcal{G}^{\mathrm{D}}_s \subseteq \mathcal{B}^{\mathrm{D}}_s$, $\mathcal{D}^{\mathrm{D}}_s \subseteq \mathcal{B}^{\mathrm{D}}_s$, $\mathcal{C}^{\mathrm{D}}_s \subseteq \mathcal{B}^{\mathrm{D}}_s$, and $\mathcal{E}^{\mathrm{D}}_s \subseteq \mathcal{B}^{\mathrm{D}}_s$, respectively. Each DN s is connected to a designated TN bus at its PCC, where energy transactions between the TN and DN s are carried out. For the DN topology, $\mathcal{P}_{i,s}$ denotes the parent bus set of bus i in DN s, and $\mathcal{C}_{i,s}$ denotes its child bus set. The scheduling horizon is discretized into time periods indexed by $t \in \mathcal{T}$. For each model $[\cdot] \in \{\mathrm{UL}, \mathrm{LL}, \mathrm{SL}\}$, the corresponding decision variables are collected in $\Xi^{[\cdot]}$, where UL, LL, and SL denote the upper-level (UL) model, lower-level (LL) model, and the single-level reformulation of the mathematical program with equilibrium constraint (MPEC) model, respectively.

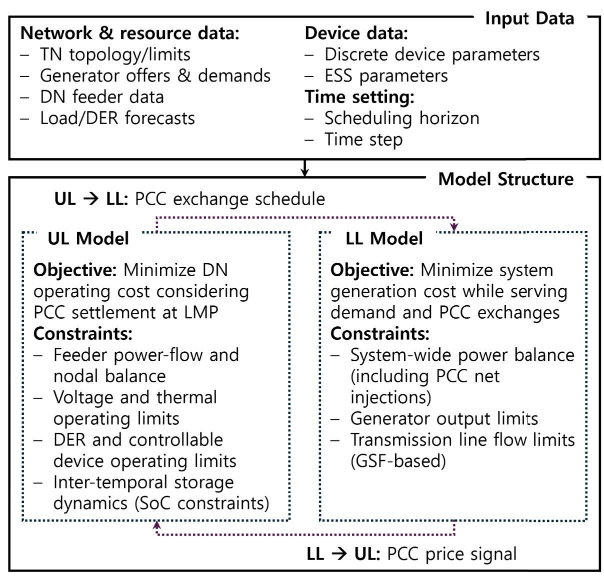

FIGURE 2. Flowchart of the bilevel TN–DN co-optimization showing inputs and outputs, objectives, and key constraints.

Fig. 2 provides a flowchart of the bilevel TN–DN co-optimization, summarizing the input data, the objective functions and key constraints of each level, and the input and output signals exchanged between the UL and LL. The bulk power system is scheduled based on generator offers and DN bids at the PCCs. This scheduling determines the optimal TN dispatch and the PCC LMPs. The TN scheduling minimizes the total operating cost of the TN. The resulting PCC LMPs serve as reference prices for energy transactions between the TN and the DNs. Each DN schedules its DERs and internal control devices. It also decides the PCC power exchange based on its bids and the PCC LMP. The PCC LMP affects the DN optimal schedule, including the PCC exchange, DER and ESS dispatch, and the settings of discrete control devices. These DN decisions, in turn, change the net

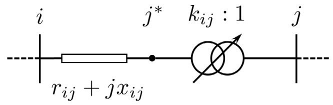

FIGURE 3. Representation of a tap-changing transformer for mathematical modeling of tap-change effects.

TABLE 2. Upper-level model nomenclature: Parameters.

$\overline{V}_{i,s}$, $\underline{V}_{i,s}$	Upper and lower bounds of voltage magnitude at bus i in DN s
$\overline{P}_{i,s}$, $\underline{P}_{i,s}$	Upper and lower bounds of active power for the DER at bus i in DN s
$\overline{Q}_{i,s}$, $\underline{Q}_{i,s}$	Upper and lower bounds of reactive power for the DER at bus i in DN s
$R_{ij,s}$, $X_{ij,s}$	Series resistance and reactance for line ij in DN s
$\overline{I}_{ij,s}$	Upper bound of current for line ij in DN s
$P^{\mathrm{d}}_{i,t,s}$, $Q^{\mathrm{d}}_{i,t,s}$	Active and reactive power demand at bus i at time t in DN s
$C_{i,t,s}$	Offer price for the active power output of the DER at bus i in DN s at time t
$\overline{T}_{ij,s}$, $\underline{T}_{ij,s}$	Upper and lower bounds of tap ratio for the tap changer on line ij in DN s
$N^{pos}_{ij,s}$	Number of tap positions for the tap changer on line ij in DN s
$N^{tap}_{ij,s}$	Maximum number of tap changes over the scheduling horizon for the tap changer on line ij in DN s
$L_{ij,s}$	Length of the binary representation of the tap position for the tap changer on line ij in DN s
$\overline{K}^{\mathrm{c}}_{i,s}$	Total number of switchable stages of the CB installed at bus i in DN s
$Q^{\mathrm{c}}_{i,s}$	Reactive power capacity of the CB at bus i in DN s
$L^{\mathrm{c}}_{i,s}$	Length of the binary representation of the number of switched-on stages of the CB at bus i in DN s
$N^{cap}_{i,s}$	Maximum number of switching actions over the horizon of the CB at bus i in DN s
$\overline{P}^{\mathrm{e}}_{i,s}$	Rated charge and discharge power limit of the ESS at bus i in DN s
$\overline{SoC}_{i,s}$, $\underline{SoC}_{i,s}$	Upper and lower bounds of SoC of the ESS at bus i in DN s
$\eta^{ch}_{i,s}$, $\eta^{\mathrm{dis}}_{i,s}$	Charging and discharging efficiencies of the ESS at bus i in DN s
$E_{i,s}$	Energy capacity of the ESS at bus i in DN s
Δt	Scheduling time interval

Note: For Tables 2–7, electrical quantities are in p.u., prices are in \$/MWh, and Δt is in h. Tap positions, switching limits, efficiencies, and SoC are dimensionless.

injection at the PCC and can therefore influence the PCC LMP. This interdependency motivates a modeling framework that co-determines PCC LMPs and PCC exchanges under DN-feasible operation.

B. MATHEMATICAL FORMULATION

This subsection formulates the coordinated transmission–distribution operation as a bi-level optimization problem. The UL represents the optimal operation of DNs equipped with discrete voltage control devices and ESSs, while determining the active-power transaction at the PCC. The LL corresponds to the TN optimal dispatch problem based on a generation shift factor (GSF)-based DC-OPF, which determines the TN dispatch and the PCC LMPs. The two levels are coupled through the PCC exchange and the resulting PCC LMP. The variable $p_{0,t,s}$ represents this PCC active-power exchange in

TABLE 3. Upper-level model nomenclature: Variables.

Continuous Variable	
$p_{i,t,s}$, $q_{i,t,s}$	Active and reactive power of the DER at bus i in DN s at time t; for $i=0$, it represents net active and reactive power at the substation of DN s.
$v_{i,t,s}$	Squared voltage magnitude at bus i in DN s at time t
$v_{j^*,t,s}$	Squared voltage magnitude at auxiliary bus j^* for tap-changer modeling
$p_{ij,t,s}$, $q_{ij,t,s}$	Active and reactive power flow for line ij in DN s at time t
$\ell_{ij,t,s}$	Squared current magnitude for line ij in DN s at time t
$k_{ij,t,s}$	Tap ratio of the tap changer for line ij in DN s at time t determined by tap position $c_{ij,t,s}$
$q^{\mathrm{c}}_{i,t,s}$	Reactive power injection from the switched-on CB stages at bus i in DN s at time t determined by $k^{\mathrm{c}}_{i,t,s}$
$p^{\mathrm{e}}_{i,t,s}$	Net active power for the ESS at bus i in DN s at time t
$p^{\mathrm{ch}}_{i,t,s}$, $p^{\mathrm{dis}}_{i,t,s}$	Charging and discharging active power for the ESS at bus i in DN s at time t
$SoC_{i,t,s}$	SoC of the ESS at bus i in DN s at time t
Integer Variable	
$c_{ij,t,s}$	Tap position of the tap changer for line ij in DN s at time t
$k^{\mathrm{c}}_{i,t,s}$	Number of switched-on stages of the CB at bus i in DN s at time t
$u^{\mathrm{e}}_{i,t,s}$	Binary variable indicating the charging or discharging state of the ESS at bus i in DN s at time t; $u^{\mathrm{e}}_{i,t,s}=1$ if charging, $u^{\mathrm{e}}_{i,t,s}=0$ if discharging.

both levels, where a positive value indicates import from the TN to DN s, and a negative value indicates export to the TN.

1) UPPER-LEVEL MODEL

The DN minimizes its total operating cost, including the net payment for energy exchanged at the PCC, settled at the PCC LMP, and the offer-based cost of DN-connected DERs. In this paper, distribution-side DERs are PV units and are modeled as continuous dispatch variables with curtailment, without unit commitment decisions. The problem is formulated as follows:

$$\min_{\Xi^{\mathrm{UL}}} \sum_{t\in\mathcal{T}}\sum_{s\in\mathcal{I}}\left(\pi^{\mathrm{LMP}}_{0,t,s}p_{0,t,s}+\sum_{i\in\mathcal{G}^{\mathrm{D}}_s}C_{i,t,s}p_{i,t,s}\right) \tag{1a}$$

$$\text{s.t. } p_{i,t,s}+p^{\mathrm{e}}_{i,t,s}-P^{\mathrm{d}}_{i,t,s}=\sum_{j\in\mathcal{C}_{i,s}}p_{ij,t,s} - (p_{\mathcal{P}_i i,t,s}-R_{\mathcal{P}_i i,s}\ell_{\mathcal{P}_i i,t,s}),\quad i\in\mathcal{B}^{\mathrm{D}}_s,\forall t,s, \tag{1b}$$

$$q_{i,t,s}+q^{\mathrm{c}}_{i,t,s}-Q^{\mathrm{d}}_{i,t,s}=\sum_{j\in\mathcal{C}_{i,s}}q_{ij,t,s} - (q_{\mathcal{P}_i i,t,s}-X_{\mathcal{P}_i i,s}\ell_{\mathcal{P}_i i,t,s}),\quad i\in\mathcal{B}^{\mathrm{D}}_s,\forall t,s, \tag{1c}$$

$$v_{j^*,t,s}=v_{i,t,s}-2(R_{ij,s}p_{ij,t,s}+X_{ij,s}q_{ij,t,s}) + (R^2_{ij,s}+X^2_{ij,s})\ell_{ij,t,s},\quad ij\in\mathcal{L}^{\mathrm{D}}_s,\forall t,s, \tag{1d}$$

$$v_{j^*,t,s}=k^2_{ij,t,s}v_{j,t,s},\quad ij\in\mathcal{L}^{\mathrm{D}}_s,\forall t,s, \tag{1e}$$

$$q^{\mathrm{c}}_{i,t,s}=\frac{k^{\mathrm{c}}_{i,t,s}}{\overline{K}^{\mathrm{c}}_{i,s}}Q^{\mathrm{c}}_{i,s},\quad i\in\mathcal{C}^{\mathrm{D}}_s,\forall t,s, \tag{1f}$$

$$p^{\mathrm{e}}_{i,t,s}=p^{\mathrm{dis}}_{i,t,s}-p^{\mathrm{ch}}_{i,t,s},\quad i\in\mathcal{E}^{\mathrm{D}}_s,\forall t,s, \tag{1g}$$

$$0\le p^{\mathrm{ch}}_{i,t,s}\le u^{\mathrm{e}}_{i,t,s}\overline{P}^{\mathrm{e}}_{i,s},\quad i\in\mathcal{E}^{\mathrm{D}}_s,\forall t,s, \tag{1h}$$

$$0 \leq p^{\mathrm{dis}}_{i,t,s} \leq (1 - u^{\mathrm{e}}_{i,t,s})\overline{P}^{\mathrm{e}}_{i,s}, \quad i \in \mathcal{E}^{\mathrm{D}}_s, \forall t, s, \tag{1i}$$

$$SoC_{i,t,s} = SoC_{i,t-1,s} + (\eta^{ch}_{i,s} p^{ch}_{i,t,s} - \frac{p^{\mathrm{dis}}_{i,t,s}}{\eta^{\mathrm{dis}}_{i,s}})\frac{\Delta t}{E_{i,s}}, \quad i \in \mathcal{E}^{\mathrm{D}}_s, \forall t, s, \tag{1j}$$

$$\underline{SoC}_{i,s} \leq SoC_{i,t,s} \leq \overline{SoC}_{i,s}, \quad i \in \mathcal{E}^{\mathrm{D}}_s, \forall t, s, \tag{1k}$$

$$0 \leq \ell_{ij,t,s} \leq \overline{I}^2_{ij,s}, \quad ij \in \mathcal{L}^{\mathrm{D}}_s, \forall t, s, \tag{1l}$$

$$\underline{V}^2_{i,s} \leq v_{i,t,s} \leq \overline{V}^2_{i,s}, \quad i \in \mathcal{B}^{\mathrm{D}}_s, \forall t, s, \tag{1m}$$

$$\underline{P}_{i,s} \leq p_{i,t,s} \leq \overline{P}_{i,s}, \quad i \in \mathcal{G}^{\mathrm{D}}_s, \forall t, s, \tag{1n}$$

$$\underline{Q}_{i,s} \leq q_{i,t,s} \leq \overline{Q}_{i,s}, \quad i \in \mathcal{G}^{\mathrm{D}}_s, \forall t, s, \tag{1o}$$

$$\left\| \begin{matrix} 2p_{ij,t,s} \\ 2q_{ij,t,s} \\ \ell_{ij,t,s} - v_{i,t,s} \end{matrix} \right\|_2 \leq \ell_{ij,t,s} + v_{i,t,s}, \quad ij \in \mathcal{L}^{\mathrm{D}}_s, \forall t, s, \tag{1p}$$

where $\Xi^{\mathrm{UL}} := \{p_{i,t,s}, q_{i,t,s}, v_{i,t,s}, v_{i^*,t,s}, p_{ij,t,s}, q_{ij,t,s}, \ell_{ij,t,s}, q^{\mathrm{c}}_{i,t,s}, k^{\mathrm{c}}_{i,t,s}, k_{ij,t,s}, p^{\mathrm{e}}_{i,t,s}, p^{ch}_{i,t,s}, p^{\mathrm{dis}}_{i,t,s}, u^{\mathrm{e}}_{i,t,s}, SoC_{i,t,s}\}$.

The objective function (1a) minimizes the operating cost of the DNs, including the net cost of power exchange with the TN and from the DERs connected to the DNs. Constraints (1b)–(1p) represent those of the DNs, which are based on a standard SOCP-based branch-flow AC-OPF formulation and incorporate distribution-level control devices. Among them, the operation of the tap changer connected to a branch, which adjusts the secondary-side voltage, is reflected in constraints (1d) and (1e) [33]. The auxiliary bus j^* is introduced between buses i and j, as shown in Fig. 3, to facilitate the modeling of the tap changer's voltage regulation operation. For branches without a tap changer, the tap ratio $k_{ij,t,s}$ is fixed to 1 as a constant. This formulation is used for both OLTCs and SVRs in the DN. The step-voltage increment is represented through the discrete tap ratio $k_{ij,t,s}$ determined by the tap position $c_{ij,t,s}$. Constraint (1f) represents the reactive power supplied by the CB, determined by the switching status of its internal stages [34]. The resulting reactive power injection from the CB is reflected in constraint (1c). The operational characteristics of the ESSs, such as charging and discharging active power and state of charge (SoC), are modeled by constraints (1g)–(1k), where $u^{\mathrm{e}}_{i,t,s}$ is a binary variable representing the charging and discharging states of the ESSs.

2) LOWER-LEVEL MODEL

This model focuses on the minimization of the TN total operating cost, encompassing the generation cost to serve the TN load and the power exchange with the DNs. The problem is formulated as follows:

$$\min_{\Xi^{LL}} \sum_{t \in \mathcal{T}} \left(\sum_{i \in \mathcal{G}^{\mathrm{T}}} C_{i,t} p_{i,t} - \sum_{s \in \mathcal{I}} C_{0,t,s} p_{0,t,s} \right) \tag{2a}$$

$$\text{s.t.} \sum_{i \in \mathcal{G}^{\mathrm{T}}} p_{i,t} - \sum_{s \in \mathcal{I}} p_{0,t,s} - \sum_{i \in \mathcal{D}^{\mathrm{T}}} P^{\mathrm{d}}_{i,t} = 0, \quad : \Upsilon_t, \quad \forall t, \tag{2b}$$

TABLE 4. Lower-level model nomenclature: Parameters.

$\overline{P}_i, \underline{P}_i$	Upper and lower bounds of active power for the generator at bus i
$\overline{F}_l$	Upper bound of active power for line l
$P^{\mathrm{d}}_{i,t}$	Active power demand at bus i at time t
γ_{li}	Generation shift factor between bus i and line l
γ_{ls}	Generation shift factor between DN interface s and TN line l
$C_{i,t}$	Offer price for the active power output of the generator at bus i at time t
$C_{0,t,s}$	Bid and offer price associated with the PCC active power exchange of DN s at time t

TABLE 5. Lower-level model nomenclature: Variables and dual-derived quantity.

Primal Variable	
$p_{i,t}$	Active power for the generator at bus i at time t
Dual Variable	
Υ_t	Dual variable for TN power balance constraint (2b) at time t
$\overline{\Phi}_{i,t}, \underline{\Phi}_{i,t}$	Dual variables for TN generator upper and lower bounds (2c) at bus i at time t
$\overline{\Psi}_{l,t}, \underline{\Psi}_{l,t}$	Dual variables for TN line upper and lower flow limits (2d) on line l at time t
Dual-Derived Quantity	
$\pi^{\mathrm{LMP}}_{0,t,s}$	LMP at the PCC of DN s at time t derived from the LL dual variables (e.g., Eq. (3))

$$\underline{P}_i \leq p_{i,t} \leq \overline{P}_i, \quad : \underline{\Phi}_{i,t}, \overline{\Phi}_{i,t}, \quad i \in \mathcal{G}^{\mathrm{T}}, \forall t, \tag{2c}$$

$$-\overline{F}_l \leq \sum_{i \in \mathcal{G}^{\mathrm{T}}} \gamma_{li} p_{i,t} - \sum_{s \in \mathcal{I}} \gamma_{ls} p_{0,t,s} - \sum_{i \in \mathcal{D}^{\mathrm{T}}} \gamma_{li} P^{\mathrm{d}}_{i,t} \leq \overline{F}_l, \quad : \underline{\Psi}_{l,t}, \overline{\Psi}_{l,t}, \quad l \in \mathcal{L}^{\mathrm{T}}, \forall t, \tag{2d}$$

$\Xi^{LL} := \{p_{i,t}\}$. In each constraint, the colon is followed by the dual variables associated with it.

In the LL model, the objective function (2a) is designed to minimize the operating cost of the TN, which means minimizing the total generation cost required to serve the TN load while accounting for the power scheduled for exchange with the DNs. Specifically, the variable $p_{0,t,s}$ is treated as a given interface schedule determined by the UL. Constraints (2b)–(2d) are formulated using a GSF-based DC-OPF approach, which captures power balance, generation limits and line flow limits in the TN. In addition, the LMPs, denoted by $\pi^{LMP}_{0,t,s}$, in the UL model can be derived from the dual variables associated with the equality and inequality constraints of the LL problem, as follows [18]:

$$\pi^{\mathrm{LMP}}_{0,t,s} = -\Upsilon_t + \sum_{l \in \mathcal{L}^{\mathrm{T}}} \gamma_{ls} \left(\underline{\Psi}_{l,t} - \overline{\Psi}_{l,t} \right). \tag{3}$$

III. SOLUTION METHODS

The proposed model not only has a hierarchical structure but also includes control devices with discrete valued control variables and quadratic terms. To address the non-convexity arising from this structure, the problem is reformulated as an MISOCP, resulting in a tractable approximation. In addition, the proposed formulation includes an SOCP-based AC-OPF

TABLE 6. Auxiliary nomenclature: Parameters.

M_1	Big-M constant for tap-changer bilinear linearization constraints (4)
M_2	Big-M constant for complementarity linearization (9)
$\Delta T_{ij,s}$	Tap-ratio step size
ρ	Penalty coefficient for SOC-tightening slack variables $\varphi_{ij,t,s}$
κ	Weight for the pre-tightening term in (13a); updated by schedule $\{\kappa_m\}_{m=1}^{M}$
$\tau_{exact}, \tau_{init}$	SOC-gap thresholds used in Algorithm 1
$\overline{K}^{it}$	Maximum number of sequential SOC refinement iterations

TABLE 7. Auxiliary nomenclature: Variables.

Continuous Variable	
$m_{ij,t,s}$	Auxiliary continuous variable for tap-changer linearization (4)
$x_{ij,n,t,s}, y_{ij,n,t,s}$	Auxiliary continuous variables for bilinear terms with tap digits (4)
$d_{ij,t,s}$	Auxiliary nonnegative variable for tap-change counting
$d^{c}_{i,t,s}$	Auxiliary nonnegative variable for switch counting
$\varphi_{ij,t,s}$	Nonnegative slack variable for sequential SOC-tightening constraint (12d)
Integer Variable	
$u_{ij,n,t,s}$	Binary digit variable for tap position encoding on branch ij (4)–(5)
$u^{c}_{i,n,t,s}$	Binary digit variable for CB stage encoding at bus i (6)–(7)

approach, which is implemented by relaxing quadratic constraints into SOC constraints. This convex relaxation improves tractability. It also enlarges the feasible set relative to the original problem. As a result, a nonzero SOC relaxation gap may appear and can compromise solution accuracy.

A. RELAXATION OF DISCRETE CONTROL DEVICES

1) LINEARIZATION OF THE TAP CHANGER

In this model, the incorporation of a tap changer model, characterized by discrete variables and quadratic terms, introduces non-convexity. To address this, the model is exactly linearized using a binary expansion scheme and the big-M method. Specifically, constraint (1e) is reformulated as mixed-integer linear constraints, as shown below [33]:

$$v_{j^*,t,s} = \underline{T}_{ij,s} m_{ij,t,s} + \Delta T_{ij,s} \sum_{n=0}^{L_{ij,s}} 2^n x_{ij,n,t,s}, \quad ij \in \mathcal{L}_s^{\mathrm{D}}, \forall t, s, \tag{4a}$$

$$0 \le m_{ij,t,s} - x_{ij,n,t,s} \le M_1(1 - u_{ij,n,t,s}), \quad ij \in \mathcal{L}_s^{\mathrm{D}}, \forall n, t, s, \tag{4b}$$

$$0 \le x_{ij,n,t,s} \le M_1 u_{ij,n,t,s}, \quad ij \in \mathcal{L}_s^{\mathrm{D}}, \forall n, t, s, \tag{4c}$$

$$m_{ij,t,s} = \underline{T}_{ij,s} v_{j,t,s} + \Delta T_{ij,s} \sum_{n=0}^{L_{ij,s}} 2^n y_{ij,n,t,s}, \quad ij \in \mathcal{L}_s^{\mathrm{D}}, \forall t, s, \tag{4d}$$

$$0 \le v_{j,t,s} - y_{ij,n,t,s} \le M_1(1 - u_{ij,n,t,s}), \quad ij \in \mathcal{L}_s^{\mathrm{D}}, \forall n, t, s, \tag{4e}$$

$$0 \le y_{ij,n,t,s} \le M_1 u_{ij,n,t,s}, \quad ij \in \mathcal{L}_s^{\mathrm{D}}, \forall n, t, s, \tag{4f}$$

$$\Delta T_{ij,s} = \frac{\overline{T}_{ij,s} - \underline{T}_{ij,s}}{N_{ij,s}^{\mathrm{pos}}}, \quad ij \in \mathcal{L}_s^{\mathrm{D}}, \forall s, \tag{4g}$$

$$\sum_{n=0}^{L_{ij,s}} 2^n u_{ij,n,t,s} \le N_{ij,s}^{\mathrm{pos}}, \quad ij \in \mathcal{L}_s^{\mathrm{D}}, \forall t, s, \tag{4h}$$

where M_1 denotes a sufficiently large constant, and $u_{ij,n,t,s}$ is a binary variable.

To prevent mechanical fatigue, the total number of tap changes is restricted by an upper limit $N_{ij,s}^{tap}$. The corresponding constraint $\sum_{t\in\mathcal{T}} |c_{ij,t-1,s} - c_{ij,t,s}| \le N_{ij,s}^{tap}$ contains a non-linear absolute value term, which is linearized using a non-negative auxiliary variable $d_{ij,t,s}$ as follows:

$$c_{ij,t,s} = \sum_{n=0}^{L_{ij,s}} 2^n u_{ij,n,t,s}, \quad ij \in \mathcal{L}_s^{\mathrm{D}}, \forall t, s, \tag{5a}$$

$$c_{ij,t-1,s} - c_{ij,t,s} \le d_{ij,t,s}, \quad ij \in \mathcal{L}_s^{\mathrm{D}}, \forall t, s, \tag{5b}$$

$$-(c_{ij,t-1,s} - c_{ij,t,s}) \le d_{ij,t,s}, \quad ij \in \mathcal{L}_s^{\mathrm{D}}, \forall t, s, \tag{5c}$$

$$\sum_{t\in\mathcal{T}} d_{ij,t,s} \le N_{ij,s}^{tap}, \quad ij \in \mathcal{L}_s^{\mathrm{D}}, \forall s. \tag{5d}$$

2) LINEARIZATION OF THE CB

The CB model, which involves discrete variables, can be linearized using a binary expansion scheme, similar to the tap changer model. Accordingly, constraint (1f) can be reformulated to include binary variables, as shown below:

$$q^{c}_{i,t,s} = \frac{Q^{c}_{i,s}}{\overline{K}^{c}_{i,s}} \sum_{n=0}^{L^{c}_{i,s}} 2^n u^{c}_{i,n,t,s}, \quad i \in \mathcal{C}_s^{\mathrm{D}}, \forall t, s, \tag{6a}$$

$$\sum_{n=0}^{L^{c}_{i,s}} 2^n u^{c}_{i,n,t,s} \le \overline{K}^{c}_{i,s}, \quad i \in \mathcal{C}_s^{\mathrm{D}}, \forall t, s, \tag{6b}$$

where $u^{c}_{i,n,t,s}$ is a binary variable.

Similarly, the total number of switching operations is limited to extend equipment lifespan. The corresponding non-linear constraint $\sum_{t\in\mathcal{T}} |k^{c}_{i,t-1,s} - k^{c}_{i,t,s}| \le N^{cap}_{i,s}$ is linearized using an auxiliary variable $d^{c}_{i,t,s}$:

$$k^{c}_{i,t,s} = \sum_{n=0}^{L^{c}_{i,s}} 2^n u^{c}_{i,n,t,s}, \quad i \in \mathcal{C}_s^{\mathrm{D}}, \forall t, s, \tag{7a}$$

$$k^{c}_{i,t-1,s} - k^{c}_{i,t,s} \le d^{c}_{i,t,s}, \quad i \in \mathcal{C}_s^{\mathrm{D}}, \forall t, s, \tag{7b}$$

$$-(k^{c}_{i,t-1,s} - k^{c}_{i,t,s}) \le d^{c}_{i,t,s}, \quad i \in \mathcal{C}_s^{\mathrm{D}}, \forall t, s, \tag{7c}$$

$$\sum_{t\in\mathcal{T}} d^{c}_{i,t,s} \le N^{cap}_{i,s}, \quad i \in \mathcal{C}_s^{\mathrm{D}}, \forall s, \tag{7d}$$

B. MPEC REFORMULATION

The hierarchical bi-level model is equivalently reformulated as a single-level MPEC by embedding the KKT optimality conditions of the LL model into the UL model as constraints, as follows:

$$\min_{\Xi^{SL}} \quad (1\text{ a}) \tag{8a}$$

$$\text{s.t.} \quad (1b) - (1d), (1g) - (1p), (2b) - (2d), \text{ and } (4) - (7), \tag{8b}$$

$$C_{i,t} + \Upsilon_t - \underline{\Phi}_{i,t} + \overline{\Phi}_{i,t} - \sum_{l \in \mathcal{L}^{\mathrm{T}}} \gamma_{li}(\underline{\Psi}_{l,t} - \overline{\Psi}_{l,t}) = 0, i \in \mathcal{G}^{\mathrm{T}}, \forall t, \tag{8c}$$

$$0 \le (p_{i,t} - \underline{P}_i) \perp \underline{\Phi}_{i,t} \ge 0, \quad i \in \mathcal{G}^{\mathrm{T}}, \forall t, \tag{8d}$$

$$0 \le (\overline{P}_i - p_{i,t}) \perp \overline{\Phi}_{i,t} \ge 0, \quad i \in \mathcal{G}^{\mathrm{T}}, \forall t, \tag{8e}$$

$$0 \le (\sum_{i \in \mathcal{G}^{\mathrm{T}}} \gamma_{li} p_{i,t} - \sum_{s \in \mathcal{I}} \gamma_{ls} p_{0,t,s} - \sum_{i \in \mathcal{D}^{\mathrm{T}}} \gamma_{li} P^{\mathrm{d}}_{i,t} + \overline{F}_l) \perp \underline{\Psi}_{l,t} \ge 0, \quad l \in \mathcal{L}^{\mathrm{T}}, \forall t, \tag{8f}$$

$$0 \le (-\sum_{i \in \mathcal{G}^{\mathrm{T}}} \gamma_{li} p_{i,t} + \sum_{s \in \mathcal{I}} \gamma_{ls} p_{0,t,s} + \sum_{i \in \mathcal{D}^{\mathrm{T}}} \gamma_{li} P^{\mathrm{d}}_{i,t} + \overline{F}_l) \perp \overline{\Psi}_{l,t} \ge 0, \quad l \in \mathcal{L}^{\mathrm{T}}, \forall t, \tag{8g}$$

where $\Xi^{\mathrm{SL}} := \{p_{i,t,s}, q_{i,t,s}, v_{i,t,s}, v_{i^*,t,s}, p_{ij,t,s}, q_{ij,t,s}, \ell_{ij,t,s}, q^{\mathrm{c}}_{i,t,s}, k^{\mathrm{c}}_{i,t,s}, k_{ij,t,s}, p^{\mathrm{e}}_{i,t,s}, p^{\mathrm{ch}}_{i,t,s}, p^{\mathrm{dis}}_{i,t,s}, u^{\mathrm{e}}_{i,t,s}, SoC_{i,t,s}, \pi^{\mathrm{LMP}}_{0,t,s}, p_{i,t}, m_{ij,t,s}, x_{ij,n,t,s}, u_{ij,n,t,s}, y_{ij,n,t,s}, u^{\mathrm{c}}_{i,n,t,s}, \Upsilon_t, \underline{\Phi}_{i,t}, \overline{\Phi}_{i,t}, \underline{\Psi}_{l,t}, \overline{\Psi}_{l,t}\}$.

C. TRANSFORMATION TO MISOCP

1) LINEARIZATION OF COMPLEMENTARITY CONSTRAINTS

Among the KKT conditions that constitute the reformulated MPEC model, the complementarity constraints can be linearized using a big-M method, as follows:

$$0 \le a \perp b \ge 0 \rightarrow a \ge 0, b \ge 0, a \le M_2(1-u), b \le M_2 u, \tag{9}$$

where M_2 denotes a sufficiently large constant, and u is a binary variable. By applying this transformation, constraints (8d)–(8g) can be reformulated in a linear form.

2) LINEARIZATION OF BILINEAR TERMS

To linearize the bilinear term $\pi^{\mathrm{LMP}}_{0,t,s} p_{0,t,s}$ in the objective function of the MPEC reformulation model, strong duality is applied to the LL problem. This enables the substitution of the original bilinear term with an equivalent linear expression, as the optimal objective values of the primal and dual formulations are guaranteed to coincide under strong duality. Accordingly, the objective function is reformulated as follows [18]:

$$\min_{\Xi^{SL}} \sum_{t \in \mathcal{T}} \Bigg(\sum_{i \in \mathcal{G}^{\mathrm{T}}} C_{i,t} p_{i,t} - \sum_{i \in \mathcal{G}^{\mathrm{T}}} (\underline{\Phi}_{i,t} \underline{P}_i - \overline{\Phi}_{i,t} \overline{P}_i) + \sum_{i \in \mathcal{D}^{\mathrm{T}}} P^{\mathrm{d}}_{i,t} \Big(\Upsilon_t - \sum_{l \in \mathcal{L}^{\mathrm{T}}} \gamma_{li} (\underline{\Psi}_{l,t} - \overline{\Psi}_{l,t}) \Big) + \sum_{l \in \mathcal{L}^{\mathrm{T}}} (\underline{\Psi}_{l,t} + \overline{\Psi}_{l,t}) \overline{F}_l + \sum_{s \in \mathcal{I}} \sum_{i \in \mathcal{G}^{\mathrm{D}}} C_{i,t,s} p_{i,t,s} \Bigg). \tag{10}$$

D. FINAL SINGLE-LEVEL MODEL AND ASSESSMENT OF SOC RELAXATION GAP

The SOC relaxation gap indicates a numerical deviation from the nonconvex equality in the branch-flow AC-OPF formulation, potentially affecting the exactness of the solution. For the optimal solution $\boldsymbol{x}^*$ of the proposed model, this gap is defined as shown below and is used to verify the tightness of the relaxation.

$$g_{ij,t,s}(\boldsymbol{x}^*) = \left((\ell_{ij,t,s} + v_{i,t,s}) - \left\| \begin{matrix} 2p_{ij,t,s} \\ 2q_{ij,t,s} \\ \ell_{ij,t,s} - v_{i,t,s} \end{matrix} \right\|_2 \right), \tag{11}$$

The SOCP-relaxed solution is deemed effectively exact if the gap is sufficiently small. Otherwise, a non-negligible gap necessitates additional tightening procedures.

To recover the equality of the SOC constraints in such cases, the following two convex quadratic functions are defined:

$$h_{ij,t,s}(\boldsymbol{x}) = (\ell_{ij,t,s} + v_{i,t,s})^2, \tag{12a}$$

$$r_{ij,t,s}(\boldsymbol{x}) = (2p_{ij,t,s})^2 + (2q_{ij,t,s})^2 + (\ell_{ij,t,s} - v_{i,t,s})^2. \tag{12b}$$

While constraining the difference between these functions to zero ensures exactness, doing so directly renders the problem non-convex. Therefore, a linear approximation $\bar{r}_{ij,t,s}(\boldsymbol{x}; \boldsymbol{x}^k)$, derived at the k-th iterate $\boldsymbol{x}^k$, is employed and defined as:

$$\bar{r}_{ij,t,s}(\boldsymbol{x}; \boldsymbol{x}^k) = r_{ij,t,s}(\boldsymbol{x}^k) + \nabla r_{ij,t,s}(\boldsymbol{x}^k)^{\mathrm{T}} (\boldsymbol{x} - \boldsymbol{x}^k). \tag{12c}$$

Subsequently, the tightening constraint is formulated by bounding the difference between the linearized term and the convex term using a slack variable $\varphi_{ij,t,s}$:

$$h_{ij,t,s}(\boldsymbol{x}) - \bar{r}_{ij,t,s}(\boldsymbol{x}; \boldsymbol{x}^k) \le \varphi_{ij,t,s}. \tag{12d}$$

This slack variable is then minimized in the objective function to iteratively reduce the SOC relaxation gap.

However, since the sequential tightening relies on local gradients $\nabla r_{ij,t,s}(\boldsymbol{x}^k)$, an excessive initial relaxation error may lead to convergence failure. To mitigate this, a penalty-based pre-tightening scheme is employed to suppress the initial error. The final single-level formulation, reformulated as an MISOCP to obtain a tractable approximation, is given as follows:

$$\min_{\Xi^{SL}} \quad (10) + \rho \sum_{ij,t,s} \varphi_{ij,t,s} + \kappa \sum_{ij,t,s} (\ell_{ij,t,s} + v_{i,t,s}) \tag{13a}$$

$$\text{s.t.} \quad (1b) - (1d), (1g) - (1p), (2b) - (2d), (4) - (7), (8c), (12c), \text{ and } (12d), \tag{13b}$$

$$\text{The linear form of } (8d) - -(8g), \tag{13c}$$

$$\varphi_{ij,t,s} \ge 0, \quad \forall ij, t, s, \tag{13d}$$

where $ij \in \mathcal{L}^{\mathrm{D}}, t \in \mathcal{T}, s \in \mathcal{I}$ and $\rho \ge 0$ penalizes the sequential slack variables and $\kappa \ge 0$ weights the static pre-tightening term, respectively. In the pre-tightening warm-start stage, κ is updated according to the schedule $\{\kappa_m\}_{m=1}^{M}$. In the subsequent sequential SOC refinement stage, κ is fixed.

Algorithm 1 Hybrid Penalty Pre-Tightening and Sequential SOC Refinement

Require: SOCP-relaxed model $\mathcal{M}_{\text{SOCP}}$; gap metric $\text{Gap}(\cdot)$; thresholds $\tau_{\text{exact}}, \tau_{\text{init}}$; pre-tightening penalty schedule $\{\kappa_m\}_{m=1}^{M}$ (used to update κ); penalty coefficient $\rho > 0$; maximum iterations $\overline{K}^{it}$

Ensure: Refined solution $\boldsymbol{x}$

```
Solve M_SOCP to obtain x^0
g ← Gap(x^0)
if g ≤ τ_exact then                          ▷ exactness achieved
    return x^0
end if
κ ← 0                                        ▷ default if warm-start is skipped
if g > τ_init then                           ▷ penalty-based pre-tightening
    for m = 1 to M do
        κ ← κ_m                              ▷ update κ by schedule
        Solve M_PT(κ) to obtain x̃
        g ← Gap(x̃)
        x^0 ← x̃
        if g ≤ τ_init then
            break
        end if
    end for
end if
if g ≤ τ_exact then                          ▷ exactness achieved
    return x^0
end if
for k = 0 to K̄^it − 1 do                     ▷ local linearization, fixed κ
    Build r̄(x; x^k) by first-order linearization at x^k
    Solve M_ST(x^k) to obtain x^{k+1}
    g ← Gap(x^{k+1})
    if g ≤ τ_exact then
        break
    end if
end for
return x^{k+1}
```

The comprehensive solution procedure, utilizing this formulation to ensure AC feasibility, is outlined in Algorithm 1. Here, $\mathcal{M}_{SOCP}$ denotes the baseline SOCP-relaxed single-level model. $\mathcal{M}_{PT}(\kappa_m)$ denotes the penalty pre-tightened warm-start problem obtained by applying the pre-tightening weight κ_m. $\mathcal{M}_{ST}(\boldsymbol{x}^k)$ denotes the sequential SOC refinement subproblem constructed at iterate $\boldsymbol{x}^k$ using the first-order linearization in (12c) and the slack-based tightening in (12d).

IV. CASE STUDIES

This section reports numerical results on modified IEEE test systems. Case Study I uses a T14–D33 system and compares three operating cases to verify the scheduling behavior of DN control devices and to quantify the resulting changes in DER curtailment and the PCC exchange under DN operating limits. Case Study II uses a T39–D34/D37/D123 system and compares endogenous interface pricing with a decoupled benchmark that fixes LMPs at the PCC when solving each DN, focusing on LMPs at the PCC and the PCC exchange.

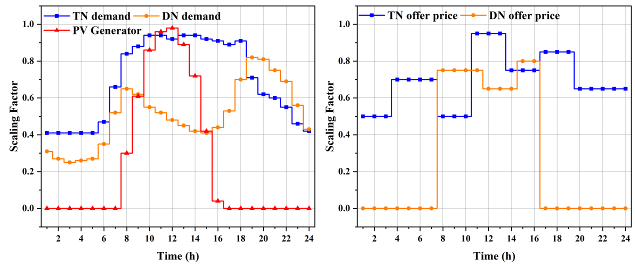

(a) (b)

FIGURE 4. Scaling factors for load, PV generation, and generator offer prices: (a) Scaling of load and PV generation based on historical data; (b) Scaling of offer prices for TN generators and DN DERs.

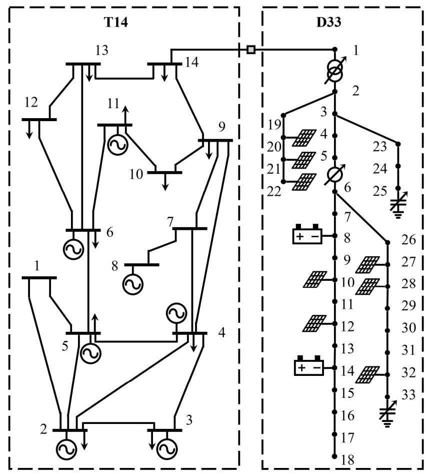

FIGURE 5. Modified IEEE 14-bus TN and 33-bus DN equipped with control devices.

A. GENERAL SIMULATION ENVIRONMENT

Each DN includes tap changers such as OLTCs and SVRs, staged CBs, and ESSs. OLTCs and SVRs have 32 tap positions with tap ratios in the range 0.95–1.05 [35]. Each CB is rated at 400 kVAr and modeled as four 100 kVAr stages [36]. To limit mechanical wear, daily tap changes are capped at 20 for each OLTC and SVR, and daily CB switching actions are capped at 10 for each CB [37]. ESS energy capacity is set to 1–2 MWh with a 0.5 C-rate, corresponding to a rated power of 0.5–1 MW. SoC is constrained to 10%–90%, and the initial and terminal SoC are fixed at 50%. Charging and discharging efficiencies are both set to 0.9. Hourly load and PV profiles are taken from [38] and [39] for a day-ahead horizon, as shown in Fig. 4. The TN line flow limit is set to 50 MW, and DN voltage magnitudes are constrained to 0.9–1.05 p.u.

The problem is formulated as an MISOCP, implemented in Python, and solved using Gurobi 12.0.1. Simulations are run on a workstation with an Intel Core i9-13900K CPU and 64 GB of RAM.

TABLE 8. Generator and PV specifications for the T14–D33 test system.

	Unit	Count	Min P (MW)	Max P (MW)	Base Offer Price ($/MWh)
TN 14	Gen.	2	10	100	35
		3	10	80	40
		2	10	50	45
DN 33	PV	2	0	3.5	15
		2	0	3.0	20
		2	0	2.0	25
		2	0	1.5	30

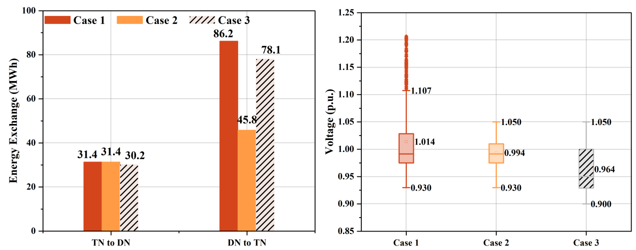

(a) (b)

FIGURE 6. Comparison of daily energy exchange and voltage profiles across simulation cases: (a) Total daily TN-to-DN and DN-to-TN energy exchange at the PCC; (b) Box plots of daily voltage magnitude distributions in the DN.

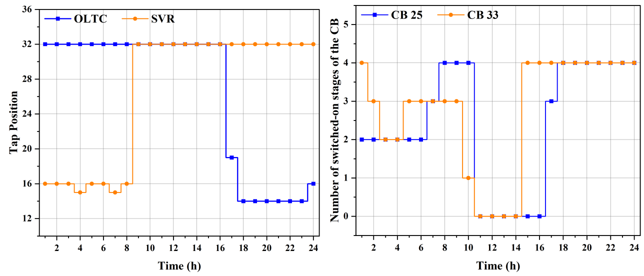

(a) (b)

FIGURE 7. Daily scheduling profiles of discrete control devices in Case 3: (a) Tap positions of the OLTC and the SVR; (b) Number of switched-on stages for the CBs at buses 25 and 33.

B. CASE STUDY I: T14–D33 SYSTEM

Fig. 5 shows the T14–D33 test system, consisting of a modified IEEE 14-bus TN and a modified IEEE 33-bus DN. The TN includes seven generators and the DN includes eight PV units, tap changers such as an OLTC and an SVR, two ESSs, and two CBs. The total rated capacities of the TN generators and DN PV units are 540 MW and 20 MW, respectively, and the peak load demands for the TN and the DN are 270 MW and 3.715 MW, respectively. Detailed generator and PV specifications are summarized in Table 8.

To separate the roles of DN network limits and discrete device scheduling, three cases are considered.

Case 1: Passive operation, DN network limits ignored.

Case 2: Passive operation, DN network limits enforced.

Case 3: Active device scheduling, DN network limits enforced.

1) ENERGY EXCHANGE BETWEEN THE TN AND THE DN

Fig. 6 summarizes daily PCC energy exchange and DN voltage distributions for Cases 1–3. The TN-to-DN energy exchange changes little across cases, staying within 30.2–31.4 MWh. In contrast, the DN-to-TN exchange is strongly affected by the voltage limit and device scheduling. Case 1 reaches 86.2 MWh but exceeds the upper-voltage limit, reaching a maximum voltage exceeding 1.2 p.u. Case 2 enforces the 1.05 p.u. limit and reduces the DN-to-TN exchange to 45.8 MWh because reverse power flow during PV hours makes the upper-voltage constraint binding, leaving PV curtailment as the primary feasibility mechanism under passive operation. Case 3 schedules DN devices and increases the DN-to-TN exchange to 78.1 MWh, recovering approximately 90% of the unconstrained capability, by coordinating DN control actions to create additional voltage headroom, thereby reducing curtailment while maintaining secure DN operation with the maximum voltage at 1.05 p.u.

The voltage distribution in Case 3 shifts downward relative to Case 2, with the median decreasing from 0.994 p.u. to 0.964 p.u., leaving additional margin under the upper-voltage constraint during PV hours. This export recovery demonstrates the operational value of actively scheduling discrete DN devices under binding DN limits.

2) OPERATION OF TAP CHANGERS AND CAPACITOR BANKS

The impact of the proposed co-optimization on system operation is evident in the voltage profiles and the corresponding device schedules illustrated in Figs. 6 and 7. As revealed in Fig. 6(b), while the severe voltage violations in Case 1 and the curtailment in Case 2 are visually reaffirmed, Case 3 successfully maintains the voltage within the 1.05 p.u. threshold while recovering energy exports through the optimized operation of discrete devices.

Fig. 7 illustrates the device co-optimization in Case 3. The discrete devices operate up to their daily switching limits of 20 for tap changers and 10 for CBs. During the PV peak between 09:00 and 16:00, the primary objective is to suppress voltage rises. To achieve this, both the OLTC and SVR maintain their maximum tap position 32. Simultaneously, the CB at Bus 33 is fully switched off and the CB at Bus 25 reduces its stages to minimize reactive power injection. This combined action counteracts the reverse power flow. Conversely, during the early morning and evening, the OLTC and SVR lower their tap positions at different times to support voltage. During the dawn hours from 00:00 to 08:00, the SVR operates at a lower tap position around 16 while the OLTC remains at the maximum tap. In the evening from 17:00 to 24:00, the OLTC lowers its tap position to around 14 whereas the SVR returns to the maximum tap. Additionally, both CBs switch to the maximum stage 4 after 18:00 to further support voltage during the peak load period. Overall, Fig. 7 indicates that tap changers and CBs are coordinated to create voltage headroom during PV hours

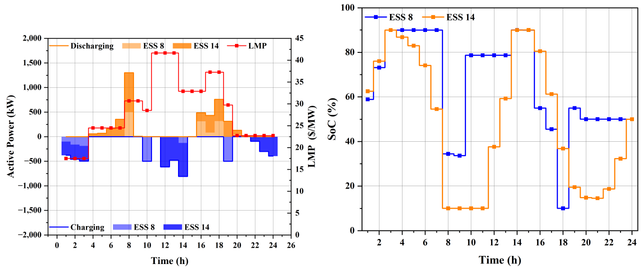

(a) (b)

FIGURE 8. ESS scheduling results with price signals: (a) Active power profiles of ESS 8 and ESS 14 plotted with the PCC LMP; (b) Daily variations of SoC.

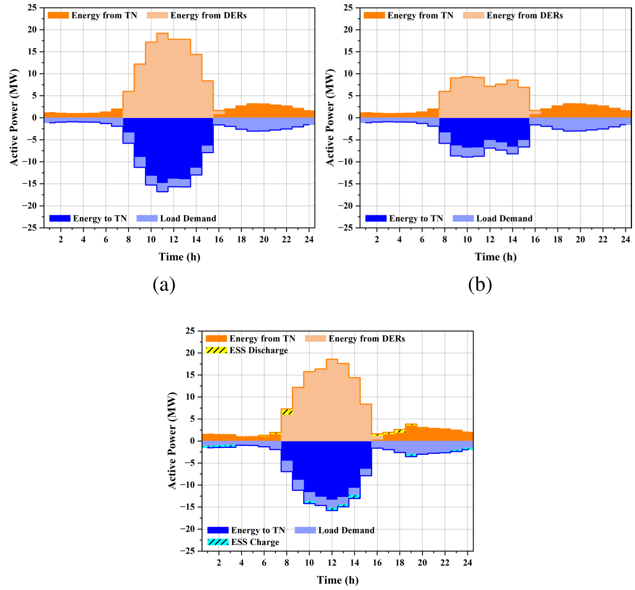

(a) (b) (c)

FIGURE 9. Comparison of daily active power balance profiles in the DN: (a) Case 1; (b) Case 2; (c) Case 3. The profiles include power from the TN, power to the TN, DER output, ESS charging and discharging, and load demand.

TABLE 9. Economic performance analysis of the DN for each simulation case over the 24-hour scheduling horizon.

	case 1	case 2	case 3
Revenue from TN ($)	3,124.82	1,609.01	2,819.37
Payment to TN ($)	896.62	896.62	854.00
Net revenue from TN ($)	2,228.20	712.39	1,965.37
Payment to DERs ($)	1,669.22	915.59	1,617.22
Net Operating Profit ($)	558.98	-203.20	348.15

and to provide voltage support during peak-load hours under practical switching limits.

3) ESS SCHEDULING UNDER PRICE SIGNALS AND DN LIMITS

Fig. 8 shows the dispatch of ESS 8 and ESS 14 against the LMP. Charging is concentrated in low-price hours overnight and in the early morning, while discharging appears in higher-price periods in the morning and evening, indicating that the ESS schedule follows arbitrage incentives when the DN is not close to its operating limits. A different behavior appears between 11:00 and 15:00. Even though the LMP is high, both ESSs shift to charging. In this interval, charging absorbs surplus PV output that would otherwise worsen voltage and loading conditions, indicating that the ESS scheduling shifts from price-driven arbitrage to constraint management when DN operating limits become binding during peak PV hours.

4) ENERGY BALANCE AND ECONOMIC ANALYSIS

Fig. 9 compares the DN active power balance across the three cases. In Case 1, PV output follows the available generation profile reaching about 20 MW and the resulting surplus is exported to the TN. In Case 2, PV output is capped at roughly 9 to 10 MW which corresponds to a 50% reduction from the available capacity. This reflects the voltage-driven curtailment and aligns with the reduced DN-to-TN exchange shown in Fig. 6(a). In Case 3, PV output is restored toward the Case 1 profile. A notable feature is the energy shifting enabled by the ESS which charges between 10:00 and 14:00 and discharges later. This operation absorbs the midday surplus and transfers energy to periods when the DN is less constrained.

Table 9 summarizes the economic impacts. These results show that active scheduling converts a feasible but loss-making operation into a profitable operation while maintaining DN voltage compliance. Case 1 yields the highest revenue but is operationally infeasible. Case 2 is feasible but results in a net operating loss of $203.20 because the binding voltage limit forces PV curtailment, reducing exported quantity and thus export revenue. Case 3 restores profitability and achieves a net operating profit of $348.15. This represents a recovery of approximately 62% of the theoretical profit observed in the unconstrained Case 1. Additionally, the payment to the TN decreases by about 4.8% from $896.62 in Case 2 to $854.00 in Case 3 as the ESS reduces purchases during high-price periods. This reduction in high-price purchases, together with reduced PV curtailment, explains the profitability recovery in Case 3.

C. CASE STUDY II: T39–D34/D37/D123 SYSTEM

Fig. 10 shows the T39–D34/D37/D123 test system, consisting of a modified IEEE 39-bus TN interfaced with three DNs based on the IEEE 34-bus, 37-bus, and 123-bus systems. Each DN includes controllable devices to manage voltage and power flows. The total rated capacity of the TN generators is 620 MW. On the DN side, the installed PV capacities are 26 MW in the 34-bus network, 26 MW in the 37-bus network, and 178 MW in the 123-bus network. Table 10 summarizes generator and PV specifications. The peak active

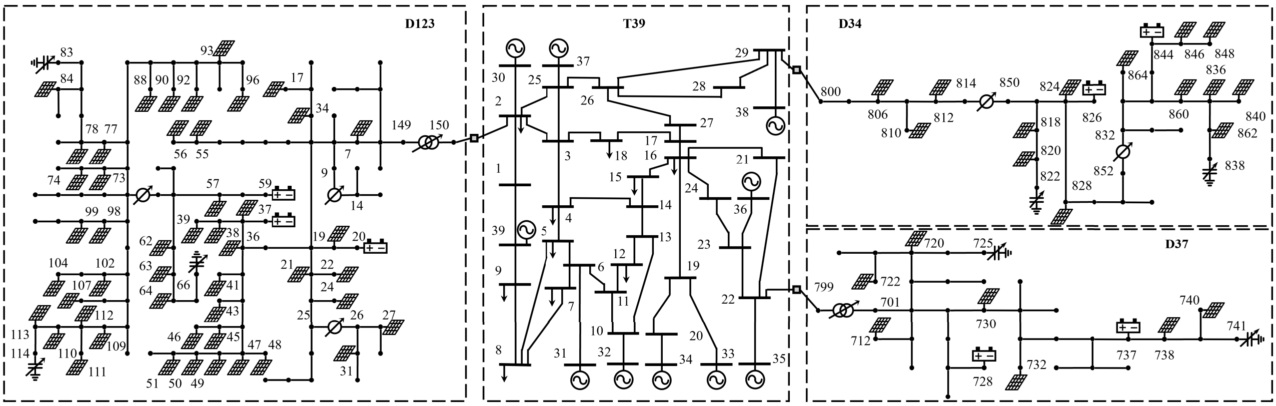

FIGURE 10. Modified IEEE 39-bus TN and 34-, 37-, and 123-bus DNs equipped with control devices.

TABLE 10. Generator and PV specifications for the T39–D34/D37/D123 test system.

	Unit	Count	Min P (MW)	Max P (MW)	Base Offer Price ($/MWh)
TN 39	Gen.	3	10	80	35
		3	10	60	40
		4	10	50	45
DN 34	PV	2	0	3.0	20
		8	0	2.0	25
		4	0	1.0	30
DN 37	PV	1	0	6.0	20
		4	0	4.0	25
		2	0	2.0	30
DN 123	PV	8	0	6.0	20
		25	0	4.0	25
		15	0	2.0	30

demand for the TN is 270 MW. For the DNs, peak active demands are 1.769 MW, 2.457 MW, and 3.49 MW, with corresponding reactive demands of 1.044 MVar, 1.201 MVar, and 1.925 MVar.

To evaluate scalability and compare co-optimization methodologies, two cases are considered. Case 4 solves transmission and distribution decisions in an endogenous co-optimization, so the PCC LMPs and PCC exchanges are mutually consistent. Case 5 represents a sequential decoupled benchmark in which the TN dispatch is determined first to obtain the PCC LMPs, and each DN then optimizes its internal schedule using those LMPs as fixed inputs.

Case 4: Endogenous interface pricing (integrated co-optimization).

Case 5: Sequential decoupled benchmark (fixed-price DN scheduling).

1) LMP AT THE PCC

Table 11 compares the PCC LMPs under Cases 4 and 5. Here, Mismatch denotes the Case 5 LMP minus the Case 4 LMP. Error denotes the corresponding percentage deviation relative to Case 4. The two profiles coincide during hours with negligible PV output from 01:00 to 09:00 and from 16:00 to 24:00. A clear divergence appears from 10:00 to 15:00, when PV output increases and the distribution net-load pattern changes. During this interval, the sequential benchmark yields consistently higher LMPs, with a maximum deviation of 4.75 $/MWh, which corresponds to 12.5%.

TABLE 11. Comparison of LMPs and price distortion at the PCC. Mismatch and error are computed relative to Case 4.

Time (h)	LMP ($/MWh)		Price Distortion	
	Case 4	Case 5	Mismatch ($/MWh)	Error (%)
9	28.00	28.00	0.00	0.00
10	26.00	29.25	+3.25	+12.50
11	38.00	42.75	+4.75	+12.50
12	38.00	42.75	+4.75	+12.50
13	38.00	42.75	+4.75	+12.50
14	30.00	33.75	+3.75	+12.50
15	30.00	33.75	+3.75	+12.50
16	33.75	33.75	0.00	0.00

TABLE 12. Comparative assessment of economic performance and market distortion at the PCC. Mismatch and ratio are computed relative to Case 4.

	case 4	case 5	Mismatch	Ratio (%)
Net Export Energy to TN (MWh)	857.71	795.25	-62.46	-7.28
Revenue from TN ($)	30,543.92	31,621.58	+1,077.66	+3.53
Payment to TN ($)	1,420.30	1,401.45	-18.85	-1.33
Net revenue from TN ($)	29,123.62	30,220.14	+1,096.51	+3.77
Payment to DERs ($)	17,376.60	16,011.31	-1,365.28	-7.86
Net Operating Profit ($)	11,747.02	14,208.82	+2,461.80	+20.96

The divergence follows from the scheduling sequence. In the sequential benchmark, TN scheduling is completed before DN feasibility and DN-side supply are incorporated. Consequently, the available energy from DN resources is not reflected in the initial optimization. This forces the system to meet demand relying solely on TN-side generation. Once lower-cost units reach their limits, a higher-cost unit

TABLE 13. Computational performance, problem size, and SOC relaxation gap for cases 1–4.

	Case 1	Case 2	Case 3	Case 4
Time (s)	0.66	94	1,061	7,885
Iter.	0	10	4	0
Cont. Var.	9,336	13,944	15,942	58,604
Bin. Var.	1,296	1,296	1,776	4,296
MIP Gap (%)	2.51	0.00	1.21	4.99
SOC Gap	$4.79 \cdot 10^{-5}$	$6.85 \cdot 10^{-8}$	$1.92 \cdot 10^{-6}$	$8.74 \cdot 10^{-4}$

becomes marginal and raises the PCC LMP. In Case 4, the co-optimization allows cost-effective DN injections to substitute for expensive TN generation, lowering the marginal cost and stabilizing the PCC LMP.

2) ECONOMIC IMPACTS AND DISTORTION METRICS

Table 12 summarizes the interface settlement outcomes. Here, Mismatch denotes Case 5 minus Case 4, and Ratio denotes the corresponding percentage deviation relative to Case 4. Relative to Case 4, Case 5 reduces the net export energy to the TN by 62.46 MWh, or 7.28%. Despite the lower exchange, the revenue from the TN increases by \$1,077.66, or 3.53%. The payment to the TN decreases by \$18.85, or 1.33%. Payments to DERs decrease by \$1,365.28, or 7.86%. The resulting calculated net operating profit increases by \$2,461.80, or 20.96%. The apparent profit increase in Case 5 reflects a settlement distortion caused by price–dispatch inconsistency.

These differences reflect the consistency between the PCC LMP and the scheduled exchange quantity under each co-optimization method. Case 4 provides an integrated benchmark in which the PCC LMP and the PCC exchange are co-determined under transmission and distribution constraints. Case 5 determines the PCC LMP in the TN scheduling stage and then determines the PCC exchange in a subsequent DN stage. When the DN schedule materially changes the marginal dispatch conditions, the sequential benchmark can produce settlement outcomes that differ from the integrated benchmark because the PCC LMP and the PCC exchange are not co-determined in the same optimization. Endogenous interface pricing co-determines them under DN-feasible operation and removes the distortions observed under the sequential benchmark as summarized in Tables 11 and 12.

D. OPTIMALITY GAP ANALYSIS OF SOC RELAXATION

This subsection evaluates the tightness of the SOCP relaxation using the SOC relaxation gap metric defined in Section III. Algorithm 1 is applied in Cases 1–4 to improve relaxation tightness. Table 13 reports the SOC relaxation gaps together with key computational statistics. In the T14–D33 cases, Cases 1 through 3, the SOC gaps range from $6.85 \cdot 10^{-8}$ to $4.79 \cdot 10^{-5}$, indicating that the SOC constraints are effectively binding in these instances. In the larger T39–D34/D37/D123 system, Case 4, the SOC gap remains well below the 10^{-3} threshold at $8.74 \cdot 10^{-4}$, confirming that the relaxation remains tight at larger scale.

When sequential SOC refinement is executed, the tightened subproblems include additional nonnegative slack variables for SOC tightening, so the number of continuous variables increases relative to the baseline relaxation. The variable counts in Table 13 correspond to the final subproblem solved by Algorithm 1 in each case. Table 13 also highlights the computational scalability of the proposed formulation. Problem size increases from 9,336 continuous variables and 1,296 binary variables in Case 1 to 58,604 continuous variables and 4,296 binary variables in Case 4, and the solution time increases from 0.66 s to 7,885 s. The sequential refinement stage terminates within 0 to 10 iterations in the reported cases, and the final mixed-integer programming (MIP) optimality gaps remain within the specified tolerance.

V. CONCLUSION

This paper developed an endogenous interface pricing framework for day-ahead transmission–distribution co-optimization in the presence of discrete distribution controls. The proposed formulation co-optimizes a DC-OPF and a branch-flow AC-OPF represented by a SOCP. LMPs at each PCC are derived endogenously from the primal–dual transmission model and are co-determined with a DN-feasible power exchange. This approach effectively addresses the price–dispatch inconsistency that arises when the DN is treated as an exogenous injection and the PCC LMP is treated as a fixed exogenous signal. Discrete voltage control devices, including tap changers and staged CBs, along with multi-period ESS scheduling, are explicitly modeled within the DNs. By enforcing KKT conditions and strong duality for the TN problem and linearizing complementarity relations, the overall co-optimization problem is reformulated as a single-level MISOCP solvable with standard mixed-integer and conic optimization solvers. The SOC relaxation gaps remained consistently below 10^{-3} across all tested cases, demonstrating that the conic relaxation was tight and the solution strategy was robust for the reported instances.

The case studies illustrated both the operational impacts of active DN device scheduling and the implications for market consistency at the interface. In the T14–D33 system, enforcing DN voltage limits without active device scheduling required substantial PV curtailment, reducing DN-to-TN exports to 45.8 MWh. In contrast, the coordinated scheduling of tap changers, CBs, and ESS increased exports to 78.1 MWh while maintaining the maximum voltage within 1.05 p.u., effectively recovering approximately 90% of the unconstrained export capability. Under the bid data and operational profiles applied in this study, this co-optimization shifted the DN outcome from a net operating loss of \$203.20 to a net operating profit of \$348.15. In the T39–D34/D37/D123 system, the sequential benchmark determining the TN dispatch first and fixing the PCC LMPs produced PCC LMP deviations of up to 4.75 \$/MWh, corresponding to

12.5%, and yielded settlement results that differed materially from the integrated benchmark. In the reported instances, the sequential benchmark reduced the net export energy to the TN by 7.28% while paradoxically increasing the calculated net operating profit by 20.96%. This outcome underscores a fundamental price–dispatch inconsistency that arises when the PCC LMP and the scheduled exchange are not determined within the same optimization process. The proposed endogenous interface pricing resolves this mismatch by co-determining the PCC LMPs and PCC exchanges, subject to transmission and distribution operating constraints.

The proposed endogenous interface pricing offers two practical advantages for distribution grid operators, system operators, and policymakers. First, it yields coordinated feeder-level schedules for discrete distribution devices and ESSs, which distribution operators can deploy as day-ahead setpoints to manage voltage and increase feasible DER exports under switching limits. Second, it yields a consistent PCC price–quantity pair, which system operators can use for day-ahead interface clearing and which policymakers and regulators can use for PCC settlement to reduce settlement distortions and incentive misalignment. Nevertheless, this work has several limitations. The TN is represented by a DC-OPF and the DN model is limited to radial feeders, without considering unbalanced or meshed operations, uncertainties, or real-time recourse. Future work will extend the TN to an AC formulation, incorporate uncertainty and reserve products, and develop scalable methods for multiple DNs while preserving price–dispatch consistency at the PCC.

REFERENCES

[1] T. Chen, Y. Song, D. J. Hill, and A. Y. S. Lam, "Enhancing flexibility at the transmission-distribution interface with power flow routers," *IEEE Trans. Power Syst.*, vol. 37, no. 4, pp. 2948–2960, Jul. 2022.

[2] N. Pourghaderi, M. Fotuhi-Firuzabad, M. Moeini-Aghtaie, M. Kabirifar, and M. Lehtonen, "Exploiting DERs' flexibility provision in distribution and transmission systems interface," *IEEE Trans. Power Syst.*, vol. 38, no. 2, pp. 1963–1977, Mar. 2023.

[3] Y. Wen, Y. Guo, Z. Hu, and G. Hug, "Quantifying and optimizing the time-coupled flexibilities at the distribution-level for TSO-DSO coordination," *IEEE Trans. Power Syst.*, vol. 40, no. 6, pp. 5071–5085, Nov. 2025.

[4] T. Tewari, A. Mohapatra, and S. Anand, "Coordinated control of OLTC and energy storage for voltage regulation in distribution network with high PV penetration," *IEEE Trans. Sustain. Energy*, vol. 12, no. 1, pp. 262–272, Jan. 2021.

[5] H. Xu, A. D. Domínguez-García, and P. W. Sauer, "Optimal tap setting of voltage regulation transformers using batch reinforcement learning," *IEEE Trans. Power Syst.*, vol. 35, no. 3, pp. 1990–2001, May 2020.

[6] Y. Guo, Q. Wu, H. Gao, S. Huang, B. Zhou, and C. Li, "Double-time-scale coordinated voltage control in active distribution networks based on MPC," *IEEE Trans. Sustain. Energy*, vol. 11, no. 1, pp. 294–303, Jan. 2020.

[7] G. C. Kryonidis, C. S. Demoulias, and G. K. Papagiannis, "A two-stage solution to the bi-objective optimal voltage regulation problem," *IEEE Trans. Sustain. Energy*, vol. 11, no. 2, pp. 928–937, Apr. 2020.

[8] Y. J. Kim, J. L. Kirtley, and L. K. Norford, "Reactive power ancillary service of synchronous DGs in coordination with voltage control devices," *IEEE Trans. Smart Grid*, vol. 8, no. 2, pp. 515–527, Mar. 2017.

[9] M. A. Medina, C. A. Coello Coello, and J. M. Ramirez, "Reactive power handling by a multi-objective teaching learning optimizer based on decomposition," *IEEE Trans. Power Syst.*, vol. 28, no. 4, pp. 3629–3637, Nov. 2013.

[10] A. M. Shaheen, R. A. El-Sehiemy, and S. M. Farrag, "Solving multi-objective optimal power flow problem via forced initialised differential evolution algorithm," *IET Gener., Transmiss. Distribution*, vol. 10, no. 7, pp. 1634–1647, May 2016.

[11] S. Habibnia, M. Faraji, M. H. Alizadeh, M. Mollayousefi Zadeh, R. Caire, G. B. Gharehpetian, and J. M. Guerrero, "Data-driven solutions for microgrids energy management systems: A state-of-the-art survey on current trends and future directions," *Renew. Sustain. Energy Rev.*, vol. 228, Mar. 2026, Art. no. 116592.

[12] J. Silva, J. Sumaili, R. J. Bessa, L. Seca, M. A. Matos, V. Miranda, M. Caujolle, B. Goncer, and M. Sebastian-Viana, "Estimating the active and reactive power flexibility area at the TSO-DSO interface," *IEEE Trans. Power Syst.*, vol. 33, no. 5, pp. 4741–4750, Sep. 2018.

[13] A. Patig, O. Stanojev, P. Aristidou, A. Kiprakis, and G. Hug, "Fast mapping of flexibility regions at TSO-DSO interfaces under uncertainty," in *Proc. IEEE PES Innov. Smart Grid Technol. Conf. Eur. (ISGT-Europe)*, Oct. 2022, pp. 1–6.

[14] M. Radi, N. Suljanovic, M. Maksič, G. Taylor, I. Pisica, and A. Souvent, "Decentralized TSO-DSO coordination for voltage regulation purposes based on renewable energy sources management–sensitivity and robustness analyses," *Electric Power Syst. Res.*, vol. 213, Dec. 2022, Art. no. 108674. [Online]. Available: https://www.sciencedirect.com/science/article/pii/S0378779622007428

[15] S. Karagiannopoulos, C. Mylonas, P. Aristidou, and G. Hug, "Active distribution grids providing voltage support: The Swiss case," *IEEE Trans. Smart Grid*, vol. 12, no. 1, pp. 268–278, Jan. 2021.

[16] A. O. Rousis, D. Tzelepis, Y. Pipelzadeh, G. Strbac, C. D. Booth, and T. C. Green, "Provision of voltage ancillary services through enhanced TSO-DSO interaction and aggregated distributed energy resources," *IEEE Trans. Sustain. Energy*, vol. 12, no. 2, pp. 897–908, Apr. 2021.

[17] H. Chen, D. Wang, R. Zhang, T. Jiang, and X. Li, "Optimal participation of ADN in energy and reserve markets considering TSO-DSO interface and DERs uncertainties," *Appl. Energy*, vol. 308, Feb. 2022, Art. no. 118319. [Online]. Available: https://www.sciencedirect.com/science/article/pii/S0306261921015749

[18] H. Chen, L. Fu, L. Bai, T. Jiang, Y. Xue, R. Zhang, B. Chowdhury, J. Stekli, and X. Li, "Distribution market-clearing and pricing considering coordination of DSOs and ISO: An EPEC approach," *IEEE Trans. Smart Grid*, vol. 12, no. 4, pp. 3150–3162, Jul. 2021.

[19] T. Jiang, C. Wu, R. Zhang, X. Li, H. Chen, and G. Li, "Flexibility clearing in joint energy and flexibility markets considering TSO-DSO coordination," *IEEE Trans. Smart Grid*, vol. 14, no. 2, pp. 1376–1387, Mar. 2023.

[20] R. Khodabakhsh, M. Haghifam, and M. S. E. Eslami, "Designing a bi-level flexibility market for transmission system congestion management considering distribution system performance improvement," *Sustain. Energy, Grids Netw.*, vol. 34, Jun. 2023, Art. no. 101000. [Online]. Available: https://www.sciencedirect.com/science/article/pii/S2352467723000085

[21] G. Tsaousoglou, R. Junker, M. Banaei, S. S. Tohidi, and H. Madsen, "Integrating distributed flexibility into TSO-DSO coordinated electricity markets," *IEEE Trans. Energy Markets, Policy Regulation*, vol. 2, no. 2, pp. 214–225, Jun. 2024.

[22] X. Wang, F. Li, J. Dong, M. M. Olama, Q. Zhang, Q. Shi, B. Park, and T. Kuruganti, "Tri-level scheduling model considering residential demand flexibility of aggregated HVACs and EVs under distribution LMP," *IEEE Trans. Smart Grid*, vol. 12, no. 5, pp. 3990–4002, Sep. 2021.

[23] J. Yin, J. Wang, J. You, H. Chen, and W. Shi, "Integrated energy system optimal operation in coal district with hydrogen heavy trucks," *Frontiers Energy Res.*, vol. 9, Sep. 2021, Art. no. 748673.

[24] S.-S. Jodeiri-Seyedian, A. Fakour, R. Nourollahi, K. Zare, B. Mohammadi-Ivatloo, and S. G. Zadeh, "Nodal pricing of renewable-oriented distribution network in the presence of EV charging stations: A hybrid robust/stochastic optimization," *J. Energy Storage*, vol. 70, Oct. 2023, Art. no. 107943.

[25] A. Fakour, S.-S. Jodeiri-Seyedian, R. Nourollahi, and K. Zare, "Bi-level integration of DSO with prosumers and parking lots under risk-based upper market involvement," *Electric Power Syst. Res.*, vol. 253, Apr. 2026, Art. no. 112521.

[26] E. Valipour, R. Nourollahi, K. Zare, and S. G. Zadeh, "A P-robust peer-to-peer framework for multi-energy microgrids in fully renewable integrated power and gas networks," *Electric Power Syst. Res.*, vol. 253, Apr. 2026, Art. no. 112525.

[27] E. Valipour, R. Nourollahi, M. T. Hagh, K. Zare, and S. G. Zadeh, "Boosting renewable hosting capacity via TCSC-enhanced transmission system planning: P-robust stochastic approach," *Renew. Energy*, vol. 258, Feb. 2026, Art. no. 124922.

[28] F. Zohrizadeh, C. Josz, M. Jin, R. Madani, J. Lavaei, and S. Sojoudi, "A survey on conic relaxations of optimal power flow problem," *Eur. J. Oper. Res.*, vol. 287, no. 2, pp. 391–409, Dec. 2020.

[29] M. Mollayousefi Zadeh, Z. Afshar, G. Farahani, and S. M. T. Bathaee, "An adaptive robust optimization model for microgrids operation using convexified AC power flow equations," *Int. Trans. Electr. Energy Syst.*, vol. 2023, Sep. 2023, Art. no. 6483030.

[30] J. Lavaei and S. H. Low, "Zero duality gap in optimal power flow problem," *IEEE Trans. Power Syst.*, vol. 27, no. 1, pp. 92–107, Feb. 2012.

[31] M. Farivar and S. H. Low, "Branch flow model: Relaxations and convexification—Part I," *IEEE Trans. Power Syst.*, vol. 28, no. 3, pp. 2554–2564, Aug. 2013.

[32] C. Coffrin, H. L. Hijazi, and P. Van Hentenryck, "The QC relaxation: A theoretical and computational study on optimal power flow," *IEEE Trans. Power Syst.*, vol. 31, no. 4, pp. 3008–3018, Jul. 2016.

[33] W. Wu, Z. Tian, and B. Zhang, "An exact linearization method for OLTC of transformer in branch flow model," *IEEE Trans. Power Syst.*, vol. 32, no. 3, pp. 2475–2476, May 2017.

[34] Y. Long and D. S. Kirschen, "Bi-level Volt/VAR optimization in distribution networks with smart PV inverters," *IEEE Trans. Power Syst.*, vol. 37, no. 5, pp. 3604–3613, Sep. 2022.

[35] S. Satsangi and G. B. Kumbhar, "Effect of load models on energy loss reduction using volt-VAR optimization," in *Proc. Nat. Power Syst. Conf. (NPSC)*, Dec. 2016, pp. 1–6. [Online]. Available: https://www.iitk.ac.in/npsc/Papers/NPSC2016/1570291742.pdf

[36] M. G. Damavandi, V. Krishnamurthy, and J. R. Marti, "A comprehensive methodology for volt-VAR optimization in active smart grids," 2016, *arXiv:1609.08697*.

[37] A. Samimi and A. Kazemi, "A new approach to optimal allocation of reactive power ancillary service in distribution systems in the presence of distributed energy resources," *Appl. Sci.*, vol. 5, no. 4, pp. 1284–1309, Nov. 2015.

[38] F. Angizeh, A. Ghofrani, and M. A. Jafari, "Dataset on hourly load profiles for a set of 24 facilities from industrial, commercial, and residential end-use sectors," Rutgers The State Univ. New Jersey, New Brunswick, NJ, USA, Tech. Rep. V1, Aug. 2020, doi: 10.17632/rfnp2d3kjp.1.

[39] M. J. Koivisto and J. P. Murcia Leon, "Solar PV generation time series (PECD 2021 update)," Dept. Wind Energy Syst., Technical Univ. Denmark, Roskilde, Denmark, Tech. Rep., 2022, doi: 10.11583/DTU.19727239.v1.

SEUNG-GIL NOH (Student Member, IEEE) received the B.S. and M.S. degrees in electrical engineering from Jeonbuk National University, Jeon-ju, South Korea, in 2018 and 2020, respectively. He is currently pursuing the Ph.D. degree at the Graduate School of Energy Convergence in Gwangju Institute of Science and Technology (GIST), Gwangju, Korea. From 2020 to 2021, he served as a researcher at Korea Electrical Safety Corporation (KESCO). He was a visiting scholar at Lawrence Berkeley National Laboratory (LBNL), Berkeley, CA, USA, from 2024 to 2025. His research interests include power systems operations and controls, active distribution networks, distributed energy resources, artificial intelligence, and electricity markets.

MIGUEL HELENO (Senior Member, IEEE) received the M.Sc. degree in electrical engineering and computer science from the University of Porto, Porto, Portugal, and the Ph.D. degree in sustainable energy systems from the University of Porto within the MIT Portugal Program. He is currently a Staff Scientist with the Lawrence Berkeley National Laboratory, leading research and innovation projects in the areas of power systems planning and economics.

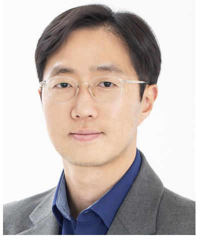

YUN-SU KIM (Senior Member, IEEE) received the B.S. and Ph.D. degrees in electrical engineering from Seoul National University, Seoul, South Korea, in 2010 and 2016, respectively. He worked for Korea Electrotechnology Research Institute (KERI) as a Senior Researcher from 2015 to 2017. He joined the Faculty of the Gwangju Institute of Science and Technology (GIST) in 2018, where he is currently a Professor with the Department of Electrical Engineering and Computer Science. He was a Fulbright Visiting Scholar at the University of Hawai'i at Mānoa, School of Law, in 2023–2024. His research interests include distribution network, distributed energy resource, microgrid, and wireless power transfer. He is an Associate Editor of IEEE Transactions on Sustainable Energy since 2023. He was a Director of the *Korean Society for New and Renewable Energy* and the *Korean Institute of Electrical Engineers*.